Journal of Advanced Ceramics
2024, **13**(10): 1600–1610
https://doi.org/10.26599/JAC.2024.9220960

Research Article

Rational design of $PrBaFe_2O_{6-\delta}$-based cathodes for protonic ceramic fuel cells

Yanru Yin[1], Shiqi Zhang[2], Ao Wang[2], Dong Yan[1], Jian Li[1], Lichao Jia[1]✉

[1] *School of Materials Science and Engineering, State Key Laboratory of Materials Processing and Die & Mould Technology, Huazhong University of Science and Technology, Wuhan 430074, China*
[2] *Wuhan Institute of Marine Electric Propulsion, Wuhan 430064, China*

Received: June 24, 2024; Revised: August 8, 2024; Accepted: August 19, 2024

Abstract: Obtaining high-performance cathodes is critical for protonic ceramic fuel cells (PCFCs), as cathode performance significantly impacts fuel cell performance. A full understanding of the interactions among the diverse properties of cathode materials would benefit cathode design. In this study, $PrBaFe_2O_{6-\delta}$ (PBF) was doped with various dopants, including cobalt (Co), Ni, Cu, Zn, and Mn. Experiments and first-principles calculations are used to study the key properties of dopant-modified $PrBaFe_2O_{6-\delta}$, including oxygen vacancy (V_O) creation, hydration ability, proton mobility, and oxygen reduction reaction (ORR) activity. There is no perfect dopant that can improve every property to its full potential. Instead, different dopants can impact different properties of the material. Co-dopant has the best cathode performance since it balances the material's instinctive properties, even though it does not provide a significant advantage in the formation of V_O. PCFC utilizing Co-doped $PrBaFe_2O_{6-\delta}$ cathode has a high performance of 1680 mW·cm^{-2} at 700 °C, which is greater than that of the other dopant-tailored $PrBaFe_2O_{6-\delta}$ cathodes reported in this study and is one of the largest ever recorded for $PrBaFe_2O_{6-\delta}$-based cathodes for PCFCs. Co-doped $PrBaFe_2O_{6-\delta}$ cathode is further demonstrated to be robust, with excellent operational stability. This study not only provides a potential cathode candidate for PCFCs but also suggests an intriguing approach to cathode design by carefully examining and balancing different vital properties of the material.

Keywords: cathode; rational design; high performance; protonic ceramic fuel cells (PCFCs)

1 Introduction

Sustainable materials and technologies have provided promising solutions to current energy and environmental problems [1,2], and different technologies have been developed in recent years [3–5]. Solid oxide fuel cells (SOFCs) have drawn considerable attention since they function as devices that effectively convert chemical energy into electrical energy [6]. The high temperatures used in conventional SOFC operation have led to problems such as difficulties in selecting sealing materials, short lifetimes, and high costs [7–9]. To enable the widespread application of SOFCs, lowering the operating temperatures of SOFCs to intermediate ranges (500–700 °C) is necessary [10,11]. Because the electrolyte used in protonic ceramic fuel cells (PCFCs) is a proton-conducting oxide [12], which typically has higher conductivity and lower activation energy than conventional oxygen-ion conducting electrolytes used in oxygen-ion conducting SOFCs (O-SOFCs) [13,14], PCFCs perform better at lower temperatures to maintain appreciable power output [15]. Thus, PCFCs play a vital role in devices that operate at intermediate temperatures [16–20], and PCFCs are also known as proton-conducting SOFCs (H-SOFCs) [21,22]. In contrast, the slow oxygen reduction reaction (ORR) activity of cathodes at low temperatures results in increased polarization resistance at lower temperatures, influencing the performance of PCFCs at intermediate temperatures [23]. Therefore, many studies have focused on creating cathode materials with high catalytic activity at intermediate temperatures [24–28].

Among the different cathode materials, double perovskites, $ReBaM_2O_{6-\delta}$ (where M is the transition metal, and Re is the element in lanthanides), have garnered much attention since they have a highly ordered layer structure created along *c*-axis by [BaO]–[MO_2]–[ReO]–[MO_2]–[BaO] [29]. This unique structure of double perovskites, which results from the large ionic radius difference between Re and Ba, allows them to perform well in surface exchange and rapid oxygen diffusion rates. This feature leads to high electronic conductivity and mixed ionic conductivity over a broad range of oxygen pressures [30]. Additionally, a number of results suggest that some double perovskite materials possess proton conductivity, making them appropriate for use as cathode materials in PCFCs [31]. Cobalt (Co)-based $PrBaCo_2O_{6-\delta}$ in $ReBaM_2O_{6-\delta}$ family has good catalytic activity and has received considerable attention [32]. However, its high thermal expansion coefficient (TEC) usually leads to dehiscence between the cathode and electrolyte, resulting in poor operational stability of fuel cells [7]. In addition, a number of issues, including Co evaporation and the high price of Co, should be addressed before its practical application [33]. In contrast, $PrBaFe_2O_{6-\delta}$ (PBF), which is known for its high chemical stability, low cost, good catalytic activity, and Co-free composition [34], provides another possible alternative as a cathode material for PCFCs.

However, Fe-based perovskite materials usually exhibit lower catalytic activity than Co-based perovskite materials do [35,36].

✉ Corresponding author.
E-mail: jialc@hust.edu.cn

Therefore, numerous methods have been implemented to increase the catalytic activity of $PrBaFe_2O_{6-\delta}$ to meet the need for PCFC cathode applications. Doping $PrBaFe_2O_{6-\delta}$ with various elements, such as Mo, Nb, W, Ga, Ta, Cu, and Zn, has been proven to be an effective way to improve fuel cell performance [30,37–42]. These studies do, however, attribute the enhanced performance to different factors. An increased oxygen vacancy (V_O) content is credited by some research for improved performance [43], whereas the optimal conductivity of oxygen or protons is suggested by others as a significant contributing factor [44]. It is not rational to attribute the improved cathode performance to only one or two factors. In reality, a variety of features may influence cathode performance. The effects of transition metals on the inherent characteristics of $PrBaFe_2O_{6-\delta}$ and their influence on PCFC cathode performance have not been thoroughly investigated. To determine the importance of these related parameters in PCFC cathode applications, $PrBaFe_2O_{6-\delta}$ is doped with representative transition metals, namely, Co, Ni, Cu, Zn, and Mn, to examine the effects of various dopants on key cathode material parameters and how these parameters affect the electrochemical performance of the cathode materials, providing a viable path for the rational design of $PrBaFe_2O_{6-\delta}$-based cathodes for PCFCs.

2 Materials and methods

Using stoichiometric ratios of the starting reagents $Pr(NO_3)_3$, $Ba(NO_3)_2$, and $Fe(NO_3)_3$, the parent material $PrBaFe_2O_{6-\delta}$ was synthesized via the traditional sol-gel method [45]. The purity of the starting reagents was determined with an analytic reagent, which was commercially available from Aladdin Reagent Co., Ltd., China. The starting reagents were mixed in a water solution, and citric acid was added. The molar ratio between the citric acid and metal cations was 1.5 : 1. After the metal nitrates and citric acid were dissolved, NH_4OH solution was slowly added until the pH of the solution reached ~8. Then, the solution was heated until it became viscous and finally flamed. The resulting precursors were then calcined in a furnace at 1000 °C for 3 h. PBFCo, PBFNi, PBFCu, PBFZn, and PBFMn are the names given to the Co, Ni, Cu, Zn, and Mn-doped $PrBaFe_2O_{6-\delta}$ materials that were synthesized via the same method. These materials were made in a stoichiometric ratio according to $PrBaFe_{1.8}Co_{0.2}O_{6-\delta}$, $PrBaFe_{1.8}Ni_{0.2}O_{6-\delta}$, $PrBaFe_{1.8}Cu_{0.2}O_{6-\delta}$, $PrBaFe_{1.8}Zn_{0.2}O_{6-\delta}$, and $PrBaFe_{1.8}Mn_{0.2}O_{6-\delta}$, with certain proportions of $Co(NO_3)_2$, $Ni(NO_3)_2$, $Cu(NO_3)_2$, $Zn(NO_3)_2$, and $Mn(NO_3)_2$ added, respectively, during the synthesis process. X-ray diffraction (XRD) was used to characterize the materials after calcination to determine phase purity. The protonation ability of these materials was investigated via thermogravimetry (TG) method. After the samples were treated with dry air at 400 to 800 °C to remove the absorbed water, they were cooled to 400 °C in a wet air atmosphere. The weight changes that were measured throughout this procedure provided information regarding the water absorption capacity of the samples. The surface proton exchange coefficient and bulk diffusion coefficient were measured via the electrical conductivity relaxation (ECR) method by changing the environment of dense bars made of samples from dry to wet air. The bars for ECR measurements were prepared via a pressing method, and the green bars were sintered at high temperatures to obtain dense bars. The sintering temperatures for PBF, PBFMn, PBFNi, PBFCo, and PBFCu bars were 1300, 1350, 1350, 1325, and 1300 °C, respectively.

With the exception of the cathode materials used in the single-cell, PCFC performance of the series of cathode materials was assessed via the identical single-cell structure of NiO–$BaCe_{0.7}Zr_{0.1}Y_{0.2}O_{3-\delta}$ (BCZY) (anode)|BCZY electrolyte|cathode materials. Through the use of co-pressing and co-sintering procedures, half-cells were produced with an anode and a dense electrolyte membrane. The weight ratio between NiO and BCZY is 3 : 2. No extra binder was used to prepare the anode. The pressures applied to the anode substrate and the bilayer were 30 and 45 MPa, respectively. The sintering temperature for the half-cell-by-layer process was 1350 °C. To reduce Ba evaporation, a powder bath was used. The cathode was then placed on the electrolyte side of the half-cell to create a single cell, followed by co-sintering at 900 °C for 10 min to produce the final complete cell needed for the fuel cell tests. Using an electrochemical workstation, the fuel cells were tested under working conditions in which the anode chamber was fed wet H_2, and the cathode was exposed to air.

Using the projected augmented wave (PAW) method and the generalized gradient approximation (GGA) with Perdew–Burke–Ernzerhof (PBE) mode implemented in the Vienna *ab initio* simulation package (VASP) [46], density functional theory (DFT) calculations were performed to reveal the intrinsic properties of the materials. The criteria used for structural optimization were Hell-Meyer-Fynman force value of 0.05 eV·Å^{-1} per atom, cutoff energy of 520 eV, and energy convergence of 10^{-5} eV per atom. (001) surface was used for the surface calculations. The thickness of the vacuum layer was 15 Å. When performing the surface calculations, the bottom four layers were fixed, and the top two layers were relaxed. Hubbard's correction was employed, with the effective U parameters (U_{eff}) of 5.3, 3.9, 6.2, 0, and 3.32 eV for Fe, Mn, Ni, Cu, and Co, respectively.

3 Results and discussions

XRD patterns of PBF, PBFMn, PBFNi, PBFCo, PBFCu, and PBFZn are presented in Fig. 1(a). Since no extra XRD peak is visible, it is evident that Cu, Co, Ni, and Mn doped PBF was effectively synthesized without any secondary phase. With respect to PBFZn, the magnified XRD pattern from 20° to 40° shows a noticeable additional peak at ~33° associated with the secondary phase, indicating the failure of full incorporation of Zn into PBF. In addition to the phase purity, there is a noticeable peak shift in XRD patterns for Cu, Co, Ni, and Mn doped PBF compared with undoped PBF, suggesting a change in the lattice parameters with different dopants. XRD rietveld refinement is used for PBF, PBFMn, PBFNi, PBFCo, and PBFCu to gain insight into the fluctuations in the lattice parameters reflected by the movement of XRD peaks and to obtain crystal structure information. Every material is refined in the crystallization of a cubic system with a space group of $pm\bar{3}m$, as indicated by the diffraction refinement patterns displayed in Fig. 1(b). The lattice parameters for PBF, PBFMn, PBFNi, PBFCo, and PBFCu are $a = b = c$ = 3.99, 3.96, 3.94, 3.93, and 3.91 Å, respectively, taking into account the reliability indicated by the reduced chi-square (χ^2) values of 1.01, 1.07, 1.31, 1.33, and 1.23. The difference in ionic radius between Fe ions and doped transition metal elements, as well as the cation ionic valence changes caused by doping, in turn, leads to variations in the lattice parameters. In addition to the experimental results, the crystal structure of these materials was also calculated via DFT calculations, as shown in Fig. 1(c). The calculated lattice parameters for PBF, PBFMn, PBFNi, PBFCo, and PBFCu are $a = b = c$ = 4.00, 3.97, 3.95, 3.93, and 3.92 Å, respectively. The lattice parameters obtained by the calculation are similar to those obtained by refinement, demonstrating the

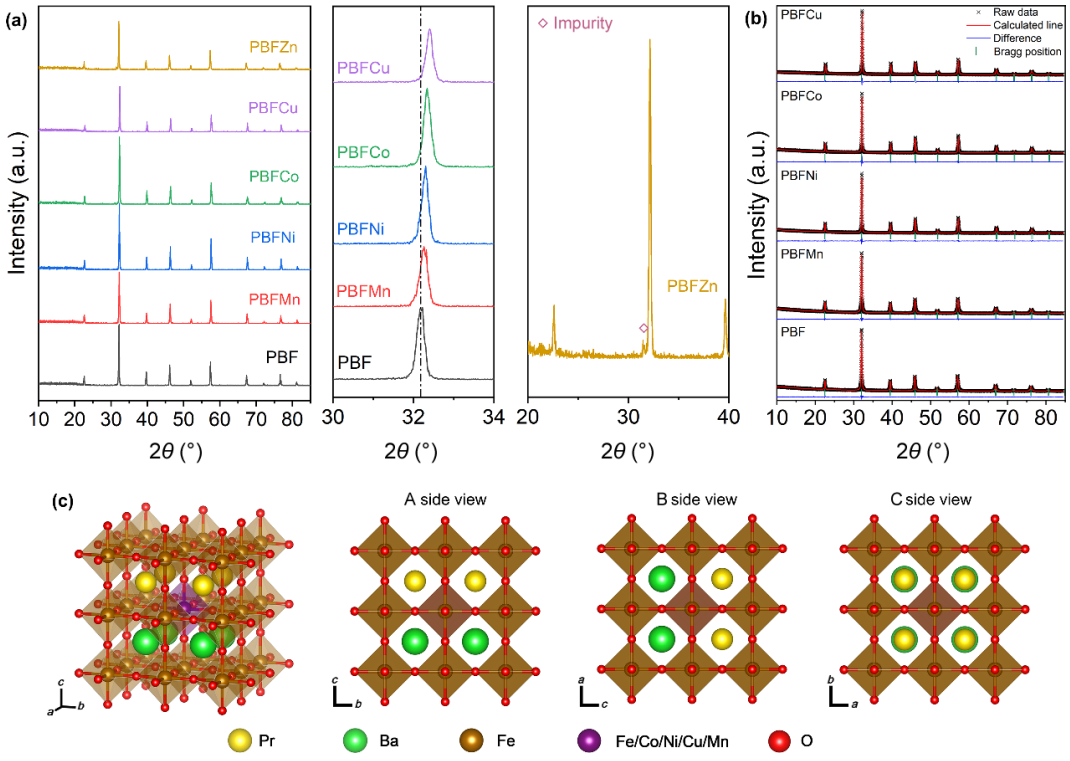

Fig. 1 (a) XRD patterns of PBF, PBFMn, PBFNi, PBFCo, PBFCu, and PBFZn. (b) Rietveld refinement for PBF, PBFMn, PBFNi, PBFCo, and PBFCu. (c) Crystal structure of $PrBaFe_{1.8}(Fe/Co/Ni/Cu/Mn)_{0.2}O_{6-\delta}$.

reliability of the simulation and providing a solid basis for the next intrinsic property simulations.

Since multiple studies have demonstrated that the presence of V_O can enhance oxygen ion transport [47,48], V_O has drawn much attention among all the factors impacting cathode material performance. Moreover, it is recognized as the pre-factor for the protonation process [49], which is another important cathodic performance evaluation metric. As a result, V_O is acknowledged in some studies as one of the most important factors influencing cathode performance [50,51]. In light of this, V_O formation energy is evaluated as the first factor considered among all of the parameters. The calculation of V_O formation energy is based on the aforementioned crystal structure and the following equation $E_{V_O} = E_{defect} + E_{O_2}/2 - E_{bulk}$ [52], where E_{V_O} represents V_O formation energy, E_{defect} represents the energy of the bulk with an oxygen vacancy, E_{O_2} represents the energy of one oxygen molecule, and E_{bulk} represents the energy of the perfect bulk. To examine the impact of the transition metal dopants, the oxygen atoms at Fe–O–M (M = Fe, Mn, Co, Ni, and Cu for PBF, PBFMn, PBFCo, PBFNi, and PBFCu) sites are selected as V_O sites. V_O locations and the associated computed results are shown in Fig. 2(a). There are different Vo sites, and different Vo sites are calculated. The site shown in Fig. 2(a) has the lowest energy, which means that this site is the most stable and has the greatest possibility for V_O formation. Given that V_O formation energy values are positive, an energy barrier must be overcome for V_O formation. In spite of this, PBFCu has the lowest V_O formation energy of 0.02 eV among all of the samples, which means that PBFCu can create V_O much more easily because there is a smaller energy barrier to overcome than other samples. In contrast, E_{V_O} for PBFMn is 0.94 eV, which is greater than that for PBF, implying that the doping strategy is not always advantageous for V_O formation. Notably, employing Ni or Co as a dopant can also enhance V_O formation even though their effects on E_{V_O} are not as significant as those on PBFCu.

V_O content of these oxides was ascertained through experimental investigations employing X-ray photoelectron spectroscopy (XPS) to validate the prediction of DFT calculations. O 1s spectra of the surface of the samples, illustrated in Fig. 2(b), can be fitted to four distinct peaks [53], which are identified as OH^-/CO_3^{2-} (hydroxyl and/or carbonate species), O_{lat} (lattice oxygen species), O_2^{2-}/O^- (highly oxidative oxygen species), and O_H (water molecule species adsorbed on the surface). According to reports, the area ratio between O_2^{2-}/O^- and O_{lat} can be used to determine the concentration of V_O on the surface [53,54]. PBF, PBFMn, PBFNi, PBFCo, and PBFCu have ratios of 0.52, 0.49, 0.60, 0.65, and 0.67, respectively. PBFCu achieves the highest V_O concentration, whereas PBFMn does not increase V_O content compared with PBF. Additionally, despite having a lower V_O content than PBFCu does, PBFCo and PBFNi yield higher V_O concentrations than PBF does. Cu, Ni, and Co dopants all increase V_O content, with Cu dopant exhibiting the most pronounced promotion, which is in agreement with DFT calculations. On the other hand, V_O formation is not enhanced by Mn dopant.

In addition to V_O concentration, the incorporation of protons for transportation is important, as this feature can extend the active area of the cathode for PCFCs [55,56]. Therefore, protonation is another important factor to consider. During the hydration process, the water molecules split into two species: H and OH. These species can then be associated with lattice oxygen and V_O, respectively [57]. As a result, the hydration ability of a material determines its protonation ability [31]. Thus, the mechanism depicted in Fig. 3(a) and the following equation are used to calculate the hydration energy of PBF, PBFMn, PBFNi, PBFCo, and PBFCu via DFT simulation $E_{hydra} = E_{2OH} - E_{defect} - E_{H_2O}$ [58], in which E_{hydra} represents the hydration energy, E_{2OH} represents the energy of the bulk with two additional

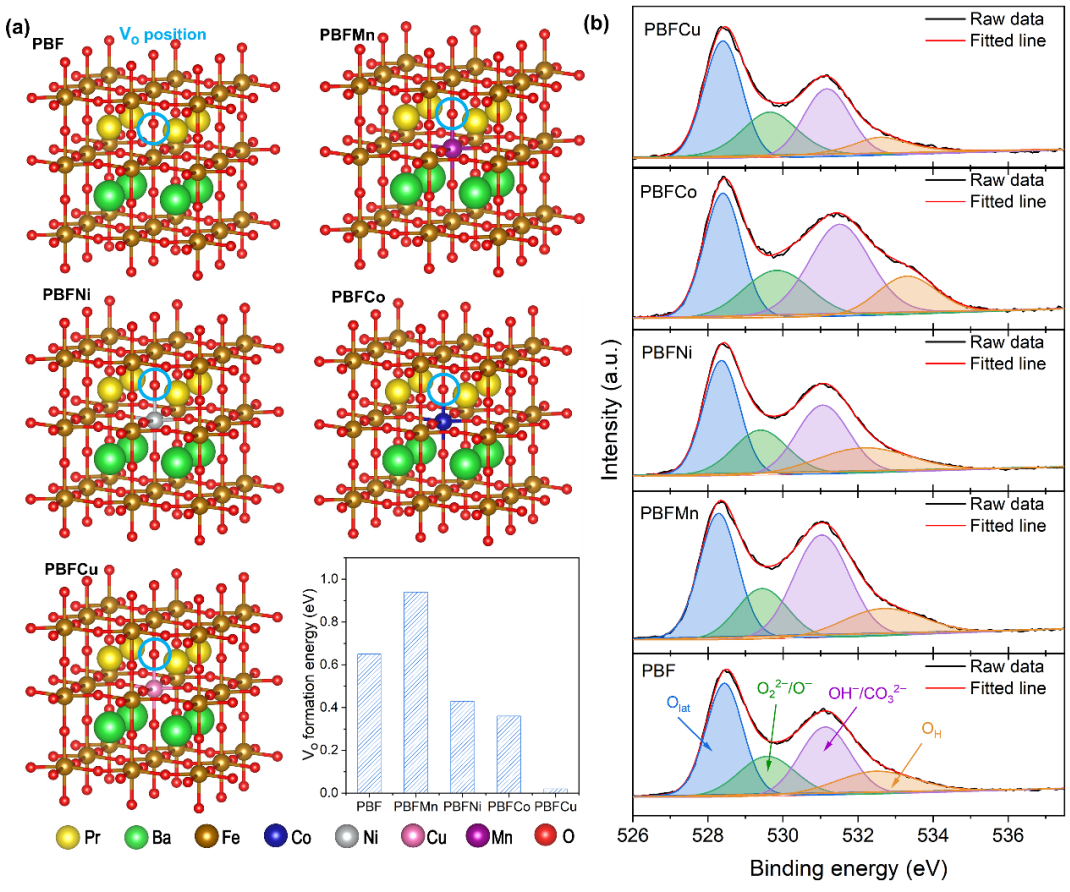

Fig. 2 (a) V_O locations and associated V_O formation energy for PBF, PBFMn, PBFNi, PBFCo, and PBFCu. (b) O 1s curves from XPS characterization.

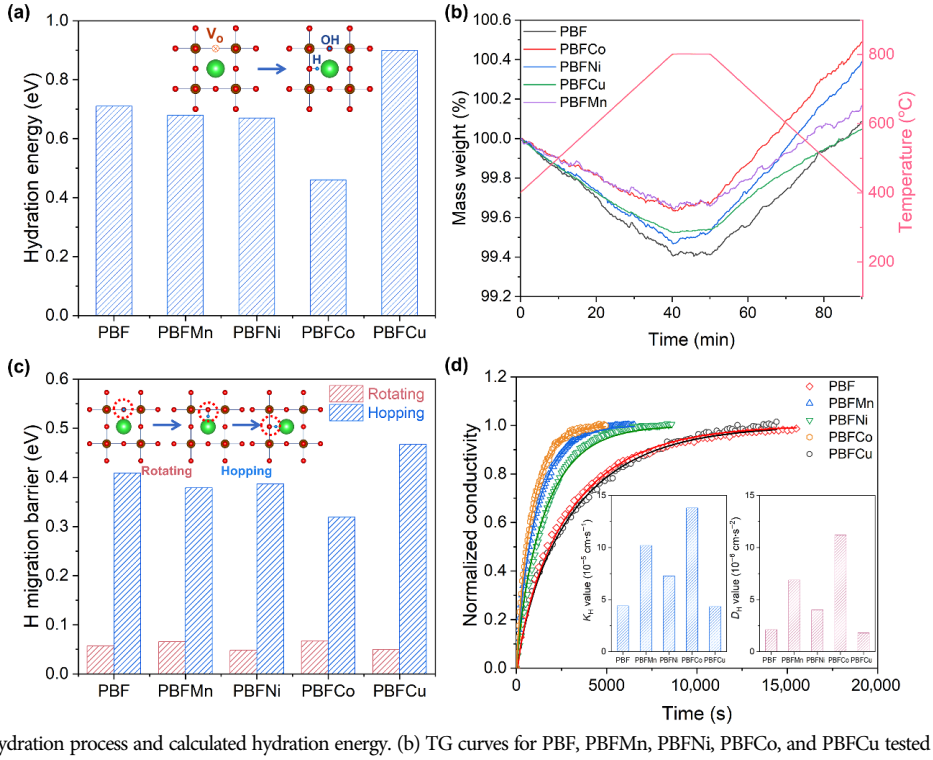

Fig. 3 (a) Scheme for hydration process and calculated hydration energy. (b) TG curves for PBF, PBFMn, PBFNi, PBFCo, and PBFCu tested in air, where water was injected into the chamber at 800 °C. (c) Scheme for proton migration and calculated energy barriers. (d) ECR curves for PBF, PBFMn, PBFNi, PBFCo, and PBFCu obtained by changing the environment from dry to wet air abruptly at 600 °C.

protons, E_{defect} represents the energy of the bulk with an oxygen vacancy, and E_{H_2O} represents the energy of one water molecule. PBF, PBFMn, PBFNi, PBFCo, and PBFCu have hydration energies of 0.71, 0.68, 0.67, 0.46, and 0.9 eV, respectively. Notably, although PBFCu produces more V_O than the other samples do, it has the highest hydration energy, suggesting that protonation in

PBFCu is a more challenging process than in other oxides and that the easy formation of V_O is not always beneficial for hydration. In contrast to PBF, PBFMn has lower hydration energy but a higher V_O formation energy, implying that the hard production of V_O does not always decrease the hydration capacity. Notably, PBFCo has the lowest hydration energy value among all the oxides under investigation, suggesting that protonation takes place more easily with the utilization of Co as the dopant than with other dopants. The protonation ability was further determined via TG measurements. The samples were exposed to dry air between 400 and 800 °C to remove the absorbed water. As dehydration occurs quickly at high temperatures, the materials are held at 800 °C to completely remove the adsorbed H_2O. Then, wet air is introduced into the atmosphere, and the materials start to absorb water. The weight gain in this process is regarded as the degree of hydration, which indicates the material's capacity for protonation [59]. PBFCo has the largest weight gain of 0.49% at 400 °C, as shown in Fig. 3(b), with the lowest hydration energy according to DFT calculations, indicating that PBFCo has the best protonation ability compared with all of the samples in this study. In contrast, PBFCu, which has the highest hydration energy, has a lower weight gain than PBF, PBFCu, PBFNi, and PBFCo, indicating that the experimental data from TG measurements and DFT simulations are consistent.

Even if protonation can be used to predict possible proton conduction behavior in oxides, the real process of proton conduction is complicated and cannot be simply linked to the degree of protonation. It has been reported that some oxides with significant protonation do not always have good proton conduction [60]. Thus, investigating the proton mobility in oxides in more detail is imperative. Protons move across oxides by rotating and hopping from one oxygen atom to an adjacent one inside the octahedron [57]. A proper concentration of the proton defect can be helpful for proton conduction, while excess proton defects may cause interactions between these defects, and proton trapping, which is detrimental to the movement of protons, can be detected [20]. Therefore, another crucial consideration when assessing the cathode materials for PCFCs is the energy barrier in the proton migration process. The proton migration mechanism and the corresponding calculated results in Fig. 3(c) show that the energy barrier in the rotation step is significantly lower than that in the hopping step for all samples, which suggests that the hopping process is the rate-limiting step in the proton migration process. The hopping energy barrier comparison reveals that PBFCo, PBFNi, and PBFMn have lower energy barriers than PBF does, whereas PBFCu has a higher energy barrier, indicating that doping with Co, Ni, and Mn is advantageous for proton migration, whereas doping with Cu deteriorates PBF's ability to transport protons because it must overcome a higher energy barrier to achieve proton mobility. DFT predictions for proton mobility are verified by ECR measurements, which provide information about an oxide's capacity for proton diffusion [61]. ECR measurement is performed by swiftly shifting the environment from dry to wet air. Proton defects appear when the samples are exposed to the environment with wet air abruptly, according to the reaction $H_2O + V_O^{\cdot\cdot} + O_O^x \rightarrow 2OH^{\cdot}$, thus affecting the conductivity of the material [61]. Both bulk proton diffusion and surface proton exchange can be reflected in the time it takes to achieve a new conductivity equilibrium after a change in the environment. Compared with PBF, which has a bulk diffusion coefficient (D_H) and surface proton exchange coefficient (K_H) of 2.12×10^{-6} $cm^2 \cdot s^{-1}$ and 4.40×10^{-5} $cm \cdot s^{-1}$, PBFCo has higher D_H and K_H values of 1.12×10^{-5} $cm^2 \cdot s^{-1}$ and 1.38×10^{-4} $cm \cdot s^{-1}$, respectively, as shown in Fig. 3(d). D_H and K_H values for PBFCo are the highest among all the tested materials. Higher K_H and D_H values are likewise displayed by PBFMn and PBFNi than by PBF, which is in line with DFT calculations. However, PBFCu has lower K_H and D_H values than PBF does, indicating that PBF with Cu doping has reduced proton diffusion abilities and surface exchange rates, which can be anticipated given the high proton migration energy barrier indicated by DFT calculations.

In addition to the abovementioned V_O formation energy, hydration energy, and proton migration energy barriers, which are correlated with the bulk model properties, surface properties also play a critical role in the evaluation of cathode performance, as a series of ORRs occur on the surface of the cathode materials [62]. As shown in Fig. 4(a), ORR process on the surface of the PCFC cathode consists of the following steps [52]: On the surface of the samples (*), O_2 molecules and H^+ adsorbed to form *OOH. It then releases an H_2O molecule by reacting with another H^+. The oxygen atom on the surface was left as *O. The remaining *O then combines with another H^+ to generate *OH, which combines with H^+ once more to release a second H_2O molecule and leaves a bare surface for the subsequent loop. Consequently, $4H^+ + O_2 \rightarrow 2H_2O$ can be used to characterize the entire reaction. Gibbs free energy of the surface, *OOH, *O, and *OH, is calculated. The results are shown in Fig. 4(b). As seen, only the energy formation of *OOH step is uphill in comparison to the other steps' downhill orientation, indicating that the formation of *OOH is the potential-limiting step of ORR in this material system. PBF, PBFMn, PBFNi, PBFCo, and PBFCu have energy barriers of 1.07, 1.1, 0.99, 0.88, and 1.18 eV, respectively. It can be concluded that compared with traditional PBF, Ni or Co doping can lower ORR energy barrier. In comparison, PBFCo has the lowest ORR energy barrier

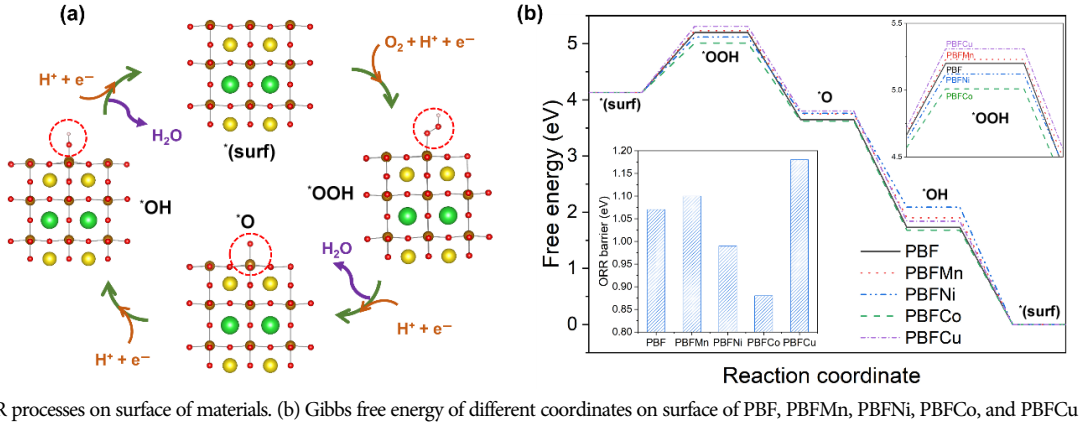

Fig. 4 (a) ORR processes on surface of materials. (b) Gibbs free energy of different coordinates on surface of PBF, PBFMn, PBFNi, PBFCo, and PBFCu at 600 °C, and corresponding energy barriers for ORR.

value of all these materials, which means that ORR activity can be enhanced more than that of the other materials by the use of Co as a dopant. Cu and Mn doping increases ORR energy barrier, which makes ORR more difficult than it would be with pristine PBF. In contrast, PBFCu has the largest ORR energy barrier, suggesting that Cu dopant presents a greater obstacle to ORR than other dopants do.

Although Cu doping increased V_O formation energy greatly, its impact on the hydration energy, proton migration energy barrier, and ORR energy barrier was unfavorable. Proton migration and hydration energy are positively impacted by Mn doping, whereas V_O formation energy and ORR energy barriers are negatively impacted. Both Ni and Co doping are optimized across the board but with a less pronounced improvement in V_O formation than Cu doping. If one were to compare Co and Ni dopants, Co would seem to be a better option for the cathode of PCFCs than Ni would be because it can improve these parameters more than Ni can. Consequently, it can be concluded that no single dopant element can achieve the best performance for every parameter. The performance of the cathode materials is the result of interactions between different factors, and the weight of these factors in the final performance needs further investigation. To determine the influence of the dopant on the cathode performance and the corresponding fuel cell performance, the electrochemical performance of PCFCs using PBF, PBFMn, PBFNi, PBFCo, and PBFCu as cathodes was evaluated.

I–V curves and a comparison of the peak power densities at various temperatures are shown in Fig. 5. PBFCo exhibited higher peak power densities of 724, 1075, and 1680 mW·cm^{-2} at 600, 650, and 700 °C, respectively, than did the fuel cell with PBF cathode, which reached 386, 568, and 1036 mW·cm^{-2} at 600, 650, and 700 °C, respectively. The results show that using Co dopant to tailor PBF is an effective tactic to improve the performance of conventional PBF cathodes. In addition to the performance being greater than that of the other PBF-based cathodes tested in this study, it is also greater than that of most Fe-based double perovskite cathode materials in PCFCs, as listed in Table 1 [44,59,61,63–68]. In contrast, PBFNi has power densities of 541, 879, and 1430 mW·cm^{-2} at 600, 650, and 700 °C, respectively. These values are lower than those of PBFCo but higher than those of the other samples. This difference can be attributed to Ni doping, which results in better performance in terms of various properties, but the extent to which it improves is lower than that of PBFCo. The power densities for PBFCu are 319, 501, and 921 mW·cm^{-2} at 600, 650, and 700 °C, respectively. While Cu doping approach can significantly increase V_O content, the fuel cell output is lower than that of PBF, suggesting that even a significant improvement in one property might not be sufficient

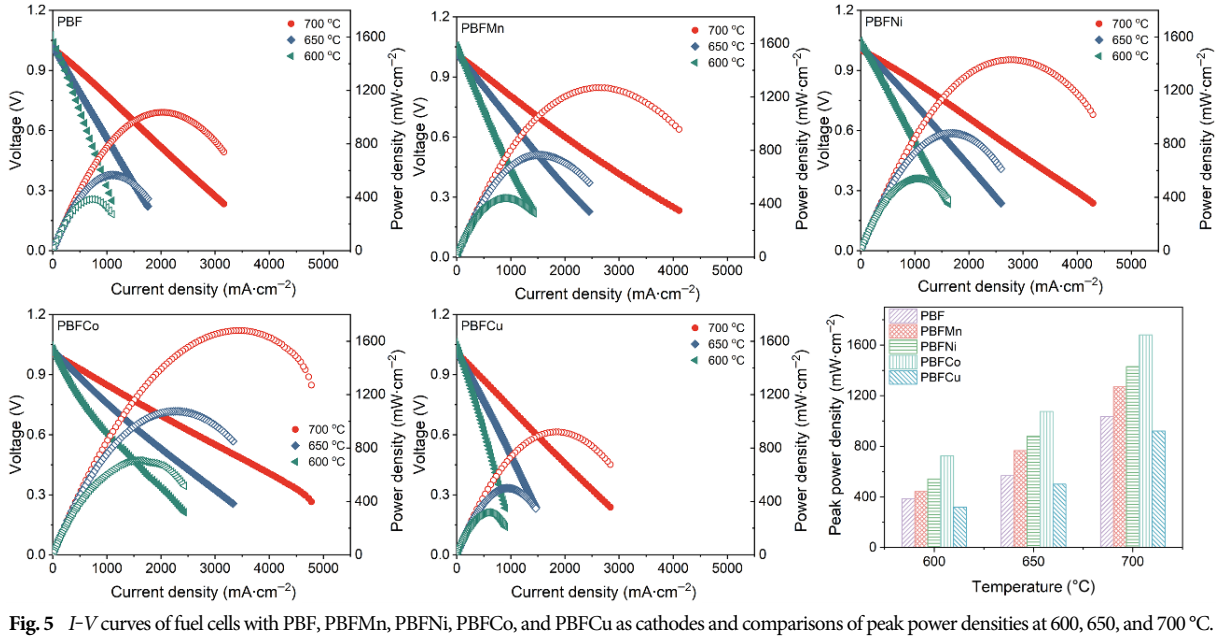

Fig. 5 *I–V* curves of fuel cells with PBF, PBFMn, PBFNi, PBFCo, and PBFCu as cathodes and comparisons of peak power densities at 600, 650, and 700 °C.

Table 1 Comparison of PCFCs' performance with Fe-based double perovskite materials as cathode at 700 °C

Cathode material	Electrolyte	Power density (mW·cm^{-2})	Ref.
$GdBaFe_2O_{5+\delta}$	BCZY	417	[63]
$PrBaCuFeO_{5+\delta}$	BCZY	445	[64]
$NdBaFe_{1.9}Mn_{0.1}O_{5+\delta}$ + BCZY	BCZY	453	[65]
$Pr_{0.5}Ba_{0.25}Sr_{0.25}FeO_{3-\delta}$ + $Sm_{0.2}Ce_{0.8}O_{2-\delta}$	BCZY	456	[66]
$SrEu_2Fe_{1.8}Co_{0.2}O_{7-\delta}$	BCZY	562	[67]
$Sr_2Fe_{1.5}Mo_{0.4}Zr_{0.1}O_{6-\delta}$	$BaZr_{0.1}Ce_{0.7}Y_{0.1}Yb_{0.1}O_3$	790	[61]
$Sr_2Fe_{1.5}Mo_{0.25}Sc_{0.25}O_{6-\delta}$	BCZY	1258	[68]
$Pr_{0.5}Ba_{0.5}$ $(Co_{0.7}Fe_{0.275}W_{0.025})O_{3-\delta}$	BCZY	1100	[44]
$PrBa_{0.9}K_{0.1}Fe_{1.9}Zn_{0.1}O_{5+\delta}$	BCZY	1400	[59]
$PrBaFe_{1.8}Co_{0.2}O_{6-\delta}$	BCZY	1680	This study

to improve the performance of the cathode material, provided that other properties deteriorate. The power densities of 443, 766, and 1270 mW·cm^{-2} at 600, 650, and 700 °C for PBFMn are higher than the fuel cell that used the pristine PBF as the cathode. The above studies have shown that while Mn doping approach results in poorer V_O formation energy and higher ORR energy barriers, it results in better hydration ability and proton migration than pristine PBF. Thus, the superior fuel cell performance with PBFMn cathode over the fuel cell with PBF cathode implies that proton migration barriers and hydration energy may play a more dominant role in the cathode performance for PCFCs. In other words, the electrochemical performance of PCFC cathode materials is influenced more by parameters related to proton conductivity, and improvements in V_O and ORR can further increase the performance, as in the case of PBFCo and PBFNi cathodes.

Notably, several studies have shown better fuel cell performance than this study. A recent study indicated that improved catalytic activity at the interface of nanocomposite cathodes can improve the cathode activity and thus increase the fuel cell output [69]. Furthermore, the performance of fuel cells is influenced not only by the cathode performance but also by the interfacial conditions. The optimization of the interfacial conditions can promote PCFC performance [70]. In addition, the testing conditions may improve cell performance. For example, the use of pure O_2 instead of air can facilitate charge diffusion and O_2 adsorption at the cathode, thus improving the performance of the cathode and fuel cell. Additionally, the current study focuses on the use of transition metal elements as dopants, which are usually used at the B site in ABO_3 perovskites. However, some dopants can be used at A site, which can also improve the performance of cathodes for PCFCs [59]. A site doping might also be an effective strategy to further promote the performance of PBF-based cathodes, deserving further investigation.

Electrochemical impedance spectroscopy (EIS) measurements were used to explore the resistance of the fuel cells, and the results are displayed in Fig. 6(a). EIS tests were performed under open circuit voltage (OCV) conditions with a frequency range from 1 MHz to 0.1 Hz. Since all of the cells use the same anode and electrolytes with similar thicknesses, it is not surprising to see that the ohmic resistance of the cells is quite close. The capacitance of EIS arc in the high-frequency range is on the order of 10^{-5} F·cm^{-2}, which is a typical response for the electrode. The value is much larger than that for the grain boundary, which is on the order of 10^{-9} F·cm^{-2}. Therefore, arc shown in EIS data is from the electrode instead of the electrolyte. The different polarization resistances corresponding to 0.130, 0.092, 0.070, 0.047, and 0.149 Ω·cm^2 are the primary reasons for the differences in the total resistances of 0.23, 0.192, 0.167, 0.143, and 0.25 Ω·cm^2 for PBF, PBFMn, PBFNi, PBFCo, and PBFCu cells, respectively, as shown in Fig. 6(b), which is associated with the power output of the full fuel cell. As shown in Fig. 6(c), scanning electron microscopy (SEM) images of the cross-sections of the fuel cells and the corresponding cathode materials indicate that all of the fuel cells and cathode materials have similar microstructures with the same electrolyte thickness of 15 μm, ruling out the possibility that the structure affects the performance of the cells and suggesting that the variation in power density is due to the inherent characteristics of the cathode materials caused by the use of various dopants.

The thermal expansion behaviors of PBF-based materials studied in this study are further investigated, and the results are shown in Fig. 7. One can see that there is no significant change in TEC values for PBF after doping with various transition metals. In the temperature range from room temperature to ~600 °C, TEC value is ~15×10^{-6} °C^{-1} for all the tested materials. In the temperature range from ~600 to 1000 °C, TEC value becomes larger for all the samples than in the low-temperature range. Comparatively, Mn and Cu doping decreases TEC, whereas Ni increases TEC. TEC of PBFCo is very close to that of PBF, being 15.94×10^{-6} °C^{-1} in the low-temperature range and 24.95×10^{-6} °C^{-1} in the high-temperature range, suggesting that a small amount of Co doping does not evidently affect TEC of PBF material.

When the abovementioned parameters are compared, PBFCo has the highest performance, indicating that it has great potential

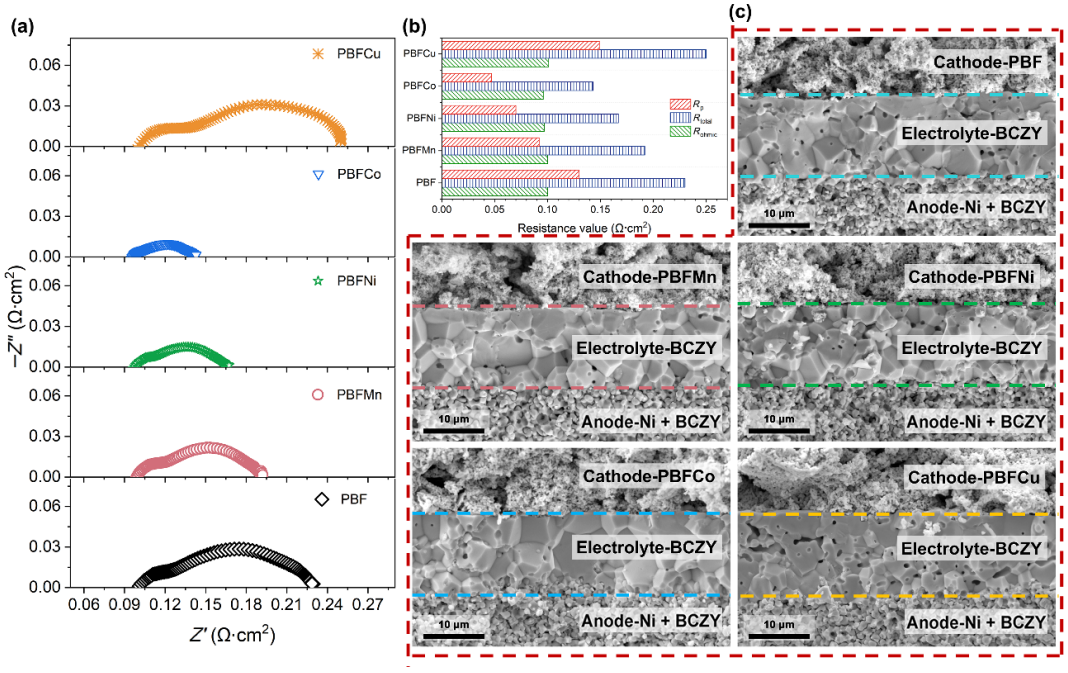

Fig. 6 (a) EIS plots tested at 700 °C for fuel cells with PBF, PBFMn, PBFNi, PBFCo, and PBFCu as cathodes, (b) comparison of resistance values at 700 °C, and (c) corresponding cross-sectional SEM images of fuel cells.

as a cathode material for the development of PCFCs. In addition to the electrochemical performance, the stability of the material should be examined. Considering that air containing some CO_2 and H_2O is produced at the cathode side of PCFCs, the stability of PBFCo in CO_2 and H_2O is tested, and the results are shown in Fig. 8. PBFCo was treated in an atmosphere containing CO_2 or H_2O at 600 °C, and XRD was used to examine the phase composition of the powder after the test. The phase of PBFCo remains unchanged after CO_2 and H_2O treatment, suggesting good stability.

Operational stability is another crucial concern that must be addressed for PCFC cathode materials to be used in practical

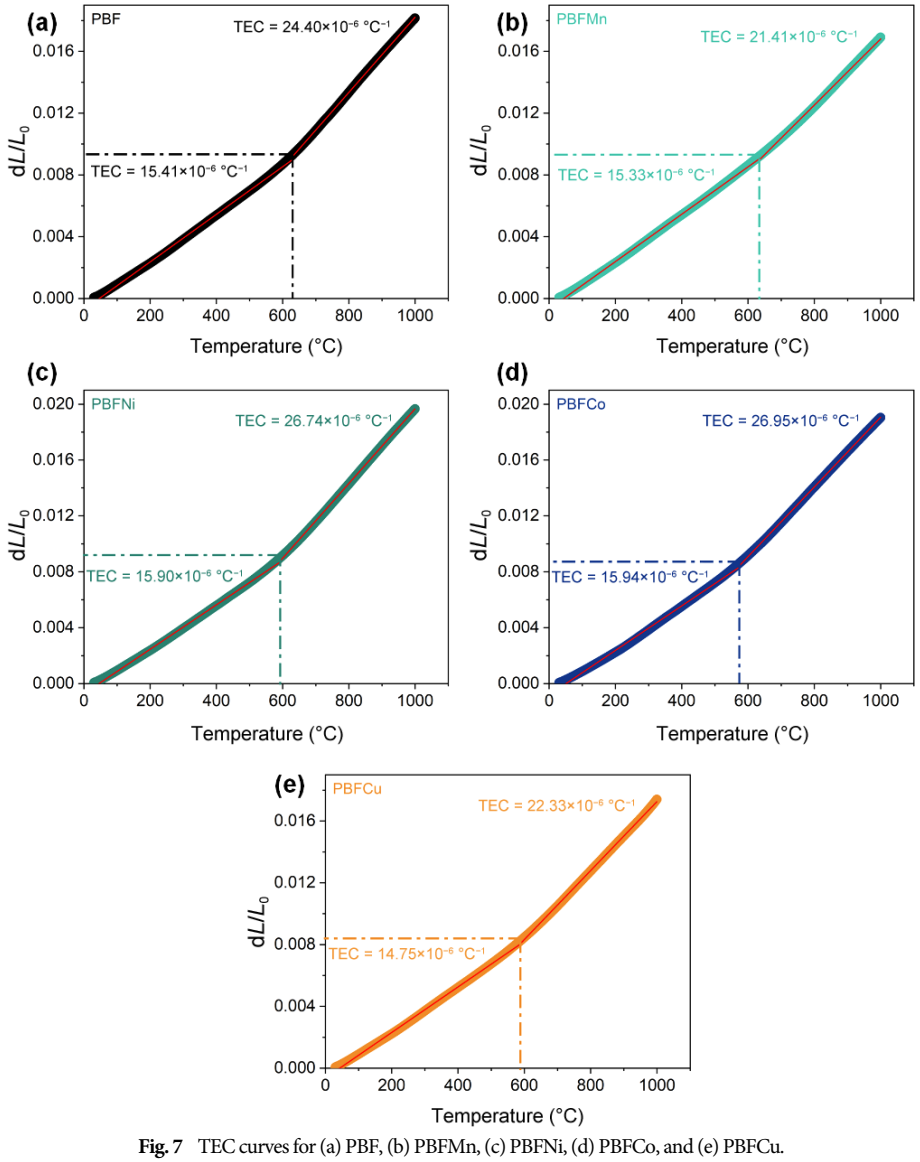

Fig. 7 TEC curves for (a) PBF, (b) PBFMn, (c) PBFNi, (d) PBFCo, and (e) PBFCu.

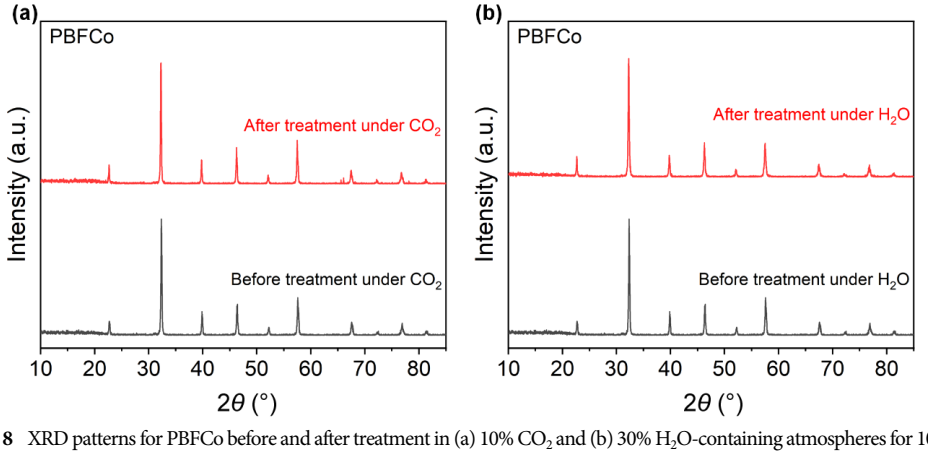

Fig. 8 XRD patterns for PBFCo before and after treatment in (a) 10% CO_2 and (b) 30% H_2O-containing atmospheres for 10 h.

applications [71,72]. Consequently, under operating conditions, the stability of the fuel cell when PBFCo is used as the cathode material is assessed. From the long-term stability test results shown in Fig. 9(a), the output voltage is maintained at ~0.85 V at 600 °C for more than 150 h without any discernible attenuation when a constant current density of 400 mA·cm^{-2} is applied, indicating good operational stability of the cell. The phase stability between PBFCo cathode and BCZY electrolyte was examined by co-firing PBFCo + BCZY composite powder at 900 °C. XRD was used to examine the phase of the powder before and after co-firing, and the results are shown in Fig. 9(b). No extra peaks can be observed, suggesting good phase stability between PBFCo and BCZY at least up to 900 °C. Following the long-term stability test, the structure and morphology of the fuel cell cross-section are investigated, and the corresponding SEM images in Fig. 9(c) reveal no structural collapse or electrolyte or cathode stripping, indicating the structural stability of the fuel cell with PBFCo as the cathode. The high fuel cell performance and good long-term stability prove that PBFCo is a robust and suitable cathode for PCFCs.

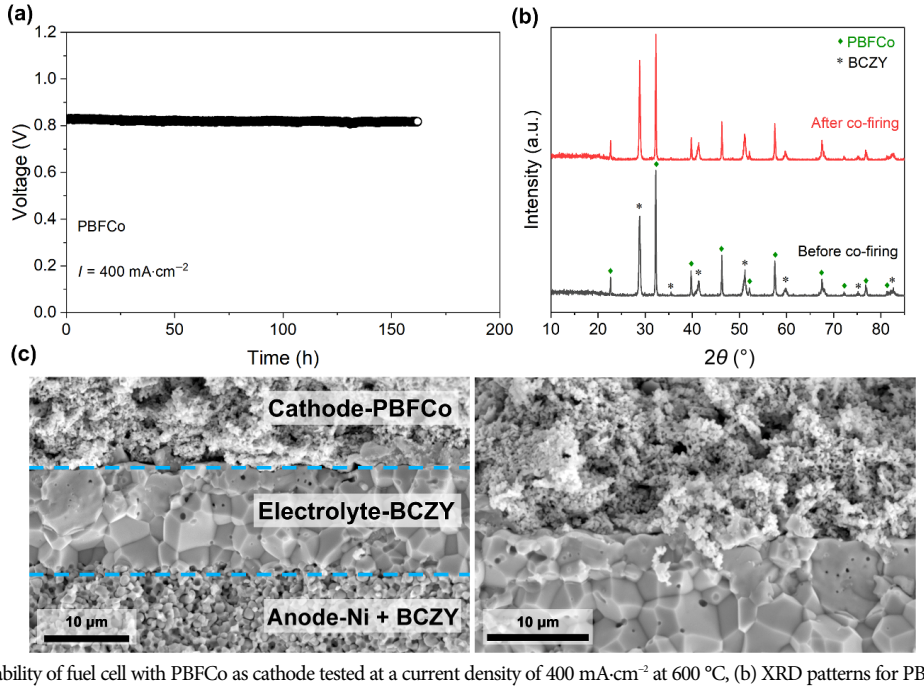

Fig. 9 (a) Long-term stability of fuel cell with PBFCo as cathode tested at a current density of 400 mA·cm^{-2} at 600 °C, (b) XRD patterns for PBFCo + BCZY before and after co-firing, and (c) cross-sectional SEM images of fuel cell after long-term stability test.

4 Conclusions

In this study, the double perovskite material PBF was chosen as a case study to evaluate the effects of various dopants on the material properties and their consequent impact on the cathode performance of PCFCs. Cu, Co, Ni, Mn, and Zn dopants were utilized to modify PBF. It was discovered that different dopants may alter material properties in different ways and that no dopant could improve all the attributes to their full potential. Zn doping resulted in impurities. Cu dopant, while significantly enhancing V_O, degraded other properties. Mn dopant, which has poor performance in ORR and V_O, improved hydration and proton migration. In comparison, Ni and Co were better alternatives since they improved V_O, ORR, hydration, and proton migration, although the improvement in V_O was not as significant as that of Cu-doped material. The use of Co dopant appeared to be a more appropriate option because it improved all the properties more than Ni dopant did, resulting in a good balance of multiple critical properties. The electrochemical investigations of fuel cells proved that PBFCo was an effective and robust cathode candidate for PCFCs, with high fuel cell output and excellent operational stability, outperforming other PBF-based cathodes in this study. The current study provided a promising cathode and, more importantly, proposed a reasonable approach to constructing high-performance cathodes for PCFCs by balancing different properties.

Acknowledgements

The authors gratefully acknowledge the financial support from the National Natural Science Foundation of China (Nos. 52072134 and 52272205), the Key Research and Development Program of Hubei Province of China (Nos. 2021BCA149 and 2022BAA087), the Natural Science Foundation for Distinguished Young Scholars of Hubei Province of China (No. 2021CFA072), and the special fund for Science and Technology Innovation Teams of Shanxi Province (No. 202304051001007). The authors would like to thank the Analytical and Testing Center of Huazhong University of Science and Technology for XRD and SEM characterizations and Sci-go (www.sci-go.com) for XPS analysis.

Declaration of competing interest

The authors have no competing interests to declare that are relevant to the content of this article.

References

[1] Zhang SJ, Lan D, Chen XL, *et al.* Three-dimensional macroscopic absorbents: From synergistic effects to advanced multifunctionalities. *Nano Res* 2024, **17**: 1952–1983.

[2] Zhu JX, Wen HY, Zhang H, *et al.* Recent advances in biodegradable electronics—From fundament to the next-generation multi-functional, medical and environmental device. *Sustain Mater Technol* 2023, **35**: e00530.

[3] Seyam S, Dincer I, Agelin-Chaab M. Environmental impact assessment of a newly developed solid oxide fuel cell-based system combined with propulsion engine using various fuel blends for cleaner operations. *Sustain Mater Technol* 2023, **35**: e00554.
[4] Niu YH, Huo WR, Yu YD, *et al.* Cathode infiltration with enhanced catalytic activity and durability for intermediate-temperature solid oxide fuel cells. *Chinese Chem Lett* 2022, **33**: 674–682.
[5] Sun JX, Ren RZ, Yue HL, *et al.* High-entropy perovskite oxide $BaCo_{0.2}Fe_{0.2}Zr_{0.2}Sn_{0.2}Pr_{0.2}O_{3-\delta}$ with triple conduction for the air electrode of reversible protonic ceramic cells. *Chinese Chem Lett* 2023, **34**: 107776.
[6] Zhang Y, Chen B, Guan DQ, *et al.* Thermal-expansion offset for high-performance fuel cell cathodes. *Nature* 2021, **591**: 246–251.
[7] Kilner JA, Burriel M. Materials for intermediate-temperature solid-oxide fuel cells. *Annu Rev Mater Res* 2014, **44**: 365–393.
[8] Han X, Ling YH, Yang Y, *et al.* Utilizing high entropy effects for developing chromium-tolerance cobalt-free cathode for solid oxide fuel cells. *Adv Funct Mater* 2023, **33**: 2304728.
[9] Zhang XX, Liu B, Yang YL, *et al.* Advances in component and operation optimization of solid oxide electrolysis cell. *Chinese Chem Lett* 2023, **34**: 108035.
[10] Zhang Y, Knibbe R, Sunarso J, *et al.* Recent progress on advanced materials for solid-oxide fuel cells operating below 500 °C. *Adv Mater* 2017, **29**: 1700132.
[11] Li C, Deng YT, Yang LP, *et al.* An active and stable hydrogen electrode of solid oxide cells with exsolved Fe–Co–Ni nanoparticles from $Sr_2FeCo_{0.2}Ni_{0.2}Mo_{0.6}O_{6-\delta}$ double-perovskite. *Adv Powder Mater* 2023, **2**: 100133.
[12] Chen M, Chen DC, Wang K, *et al.* Densification and electrical conducting behavior of $BaZr_{0.9}Y_{0.1}O_{3-\delta}$ proton conducting ceramics with NiO additive. *J Alloys Compd* 2019, **781**: 857–865.
[13] Chen M, Xie XB, Guo JH, *et al.* Space charge layer effect at the platinum anode/$BaZr_{0.9}Y_{0.1}O_{3-\delta}$ electrolyte interface in proton ceramic fuel cells. *J Mater Chem A* 2020, **8**: 12566–12575.
[14] Zvonareva IA, Mineev AM, Tarasova NA, *et al.* High-temperature transport properties of $BaSn_{1-x}Sc_xO_{3-\delta}$ ceramic materials as promising electrolytes for protonic ceramic fuel cells. *J Adv Ceram* 2022, **11**: 1131–1143.
[15] Liu ZQ, Bai YS, Sun HN, *et al.* Synergistic dual-phase air electrode enables high and durable performance of reversible proton ceramic electrochemical cells. *Nat Commun* 2024, **15**: 472.
[16] Wang Z, Wang YH, Wang J, *et al.* Rational design of perovskite ferrites as high-performance proton-conducting fuel cell cathodes. *Nat Catal* 2022, **5**: 777–787.
[17] Qiu P, Li C, Liu B, *et al.* Materials of solid oxide electrolysis cells for H_2O and CO_2 electrolysis: A review. *J Adv Ceram* 2023, **12**: 1463–1510.
[18] Liu F, Deng H, Diercks D, *et al.* Lowering the operating temperature of protonic ceramic electrochemical cells to < 450 °C. *Nat Energy* 2023, **8**: 1145–1157.
[19] Liu F, Ding D, Duan CC. Protonic ceramic electrochemical cells for synthesizing sustainable chemicals and fuels. *Adv Sci* 2023, **10**: 2206478.
[20] Yamazaki Y, Blanc F, Okuyama Y, *et al.* Proton trapping in yttrium-doped barium zirconate. *Nat Mater* 2013, **12**: 647–651.
[21] Li YF, Xu YS, Yin YR, *et al.* Entropy engineering design of high-performing lithiated oxide cathodes for proton-conducting solid oxide fuel cells. *J Adv Ceram* 2023, **12**: 2017–2031.
[22] Yang X, Yin YR, Yu SF, *et al.* Gluing $Ba_{0.5}Sr_{0.5}Co_{0.8}Fe_{0.2}O_{3-\delta}$ with Co_3O_4 as a cathode for proton-conducting solid oxide fuel cells. *Sci China Mater* 2023, **66**: 955–963.
[23] Papac M, Stevanović V, Zakutayev A, *et al.* Triple ionic–electronic conducting oxides for next-generation electrochemical devices. *Nat Mater* 2021, **20**: 301–313.
[24] Ding HP, Wu W, Jiang C, *et al.* Self-sustainable protonic ceramic electrochemical cells using a triple conducting electrode for hydrogen and power production. *Nat Commun* 2020, **11**: 1907.
[25] Qiu P, Liu B, Wu L, *et al.* K-doped $BaCo_{0.4}Fe_{0.4}Zr_{0.2}O_{3-\delta}$ as a promising cathode material for protonic ceramic fuel cells. *J Adv Ceram* 2022, **11**: 1988–2000.
[26] Yin YR, Zhou YB, Gu YY, *et al.* Successful preparation of $BaCo_{0.5}Fe_{0.5}O_{3-\delta}$ cathode oxide by rapidly cooling allowing for high-performance proton-conducting solid oxide fuel cells. *J Adv Ceram* 2023, **12**: 587–597.
[27] Liu F, Deng H, Wang ZX, *et al.* Synergistic effects of *in-situ* exsolved Ni–Ru bimetallic catalyst on high-performance and durable direct-methane solid oxide fuel cells. *J Am Chem Soc* 2024, **146**: 4704–4715.
[28] Liu F, Deng H, Ding HP, *et al.* Process-intensified protonic ceramic fuel cells for power generation, chemical production, and greenhouse gas mitigation. *Joule* 2023, **7**: 1308–1332.
[29] Dong FF, Ni M, Chen YB, *et al.* Structural and oxygen-transport studies of double perovskites $PrBa_{1-x}Co_2O_{5+\delta}$ (x = 0.00, 0.05, and 0.10) toward their application as superior oxygen reduction electrodes. *J Mater Chem A* 2014, **2**: 20520–20529.
[30] Zhang BZ, Wan YH, Hua ZH, *et al.* Tungsten-doped $PrBaFe_2O_{5+\delta}$ double perovskite as a high-performance electrode material for symmetrical solid oxide fuel cells. *ACS Appl Energy Mater* 2021, **4**: 8401–8409.
[31] Choi S, Kucharczyk CJ, Liang YG, *et al.* Exceptional power density and stability at intermediate temperatures in protonic ceramic fuel cells. *Nat Energy* 2018, **3**: 202–210.
[32] Bangwal AS, Jha PK, Dubey PK, *et al.* Porous and highly conducting cathode material $PrBaCo_2O_{6-\delta}$: Bulk and surface studies of synthesis anomalies. *Phys Chem Chem Phys* 2019, **21**: 14701–14712.
[33] Zhu ZY, Zhou MY, Fan ZD, *et al.* Improving electrocatalytic activity of cobalt-free barium ferrite-based perovskite oxygen electrodes for proton-conducting solid oxide cells via introducing A-site deficiency. *ACS Appl Energy Mater* 2023, **6**: 5155–5166.
[34] Zavyalov MA, Nikitin SS, Merkulov OV, *et al.* Influence of synthesis temperature on oxygen exchange behavior of electrode material $PrBaFe_2O_{6-\delta}$. *Solid State Ionics* 2023, **400**: 116339.
[35] Bu YF, Joo S, Zhang YX, *et al.* A highly efficient composite cathode for proton-conducting solid oxide fuel cells. *J Power Sources* 2020, **451**: 227812.
[36] Bai H, Leng ZZ, Chen T, *et al.* Synthesis and characterization of $PrBa_{0.5}Sr_{0.5}Co_{2-x}Fe_xO_{5+\delta}$ (x = 0.5, 1.0, 1.5, 2.0) as oxygen electrode for proton-conducting solid oxide cells. *Int J Hydrogen Energ* 2023, **48**: 23655–23669.
[37] Zhang HX, Yang JX, Wang PF, *et al.* Novel cobalt-free perovskite $PrBaFe_{1.9}Mo_{0.1}O_{5+\delta}$ as a cathode material for solid oxide fuel cells. *Solid State Ionics* 2023, **391**: 116144.
[38] Ding HP, Zhou DS, Liu S, *et al.* Electricity generation in dry methane by a durable ceramic fuel cell with high-performing and coking-resistant layered perovskite anode. *Appl Energ* 2019, **233–234**: 37–43.
[39] Zhang BZ, Zhang SW, Han HR, *et al.* Cobalt-free double perovskite oxide as a promising cathode for solid oxide fuel cells. *ACS Appl Mater Inter* 2023, **15**: 8253–8262.
[40] Liu CH, Wang F, Ni Y, *et al.* Ta-doped $PrBaFe_2O_{5+\delta}$ double perovskite as a high-performance electrode material for symmetrical solid oxide fuel cells. *Int J Hydrog Energ* 2023, **48**: 9812–9822.
[41] Jin FJ, Shen Y, Wang R, *et al.* Double-perovskite $PrBaCo_{2/3}Fe_{2/3}Cu_{2/3}O_{5+\delta}$ as cathode material for intermediate-temperature solid-oxide fuel cells. *J Power Sources* 2013, **234**: 244–251.
[42] Ren RZ, Wang ZH, Meng XG, *et al.* Boosting the electrochemical performance of Fe-based layered double perovskite cathodes by Zn^{2+} doping for solid oxide fuel cells. *ACS Appl Mater Inter* 2020, **12**: 23959–23967.
[43] Feng FX, Yang WY, Zheng QL, *et al.* Tuning the oxygen vacancy of the $SrSc_{0.175}Nb_{0.025}Co_{0.8}O_{3-\delta}$ cathode toward enhanced oxygen reduction reaction for H^+-SOFCs by water uptake. *Energy Fuel* 2021, **35**: 8953–8960.
[44] Tao ZT, Fu M, Liu Y, *et al.* High-performing proton-conducting solid oxide fuel cells with triple-conducting cathode of $Pr_{0.5}Ba_{0.5}(Co_{0.7}Fe_{0.3})O_{3-\delta}$ tailored with W. *Int J Hydrogen Energ* 2022, **47**: 1947–1953.

[45] Zhou R, Yin YR, Dai HL, *et al.* Attempted preparation of $La_{0.5}Ba_{0.5}MnO_{3-\delta}$ leading to an *in-situ* formation of manganate nanocomposites as a cathode for proton-conducting solid oxide fuel cells. *J Adv Ceram* 2023, **12**: 1189–1200.
[46] Kresse G, Furthmüller J. Efficient iterative schemes for *ab initio* total-energy calculations using a plane-wave basis set. *Phys Rev B* 1996, **54**: 11169–11186.
[47] Dholabhai PP. Oxygen vacancy formation and interface charge transfer at misfit dislocations in Gd-doped CeO_2/MgO heterostructures. *J Phys Chem C* 2022, **126**: 11735–11750.
[48] Huan DM, Zhang L, Zhu K, *et al.* Oxygen vacancy-engineered cobalt-free Ruddlesden–Popper cathode with excellent CO_2 tolerance for solid oxide fuel cells. *J Power Sources* 2021, **497**: 229872.
[49] Wang K, Han Y, An B, *et al.* Hydration and proton kinetics in Ce-doped Co-free perovskite for the triple-conducting cathode in solid oxide fuel cells. *J Phys Chem C* 2024, **128**: 4404–4413.
[50] Admasu Beshiwork B, Wan XY, Xu M, *et al.* A defective iron-based perovskite cathode for high-performance IT-SOFCs: Tailoring the oxygen vacancies using Nb/Ta co-doping. *J Energy Chem* 2024, **88**: 306–316.
[51] Dai HL, Du HZ, Boulfrad S, *et al.* Manipulating Nb-doped $SrFeO_{3-\delta}$ with excellent performance for proton-conducting solid oxide fuel cells. *J Adv Ceram* 2024, **13**: 579–589.
[52] Muñoz-García AB, Tuccillo M, Pavone M. Computational design of cobalt-free mixed proton–electron conductors for solid oxide electrochemical cells. *J Mater Chem A* 2017, **5**: 11825–11833.
[53] Zhang XH, Pei CL, Chang X, *et al.* FeO_6 octahedral distortion activates lattice oxygen in perovskite ferrite for methane partial oxidation coupled with CO_2 splitting. *J Am Chem Soc* 2020, **142**: 11540–11549.
[54] Yin YR, Dai HL, Yu SF, *et al.* Tailoring cobalt-free $La_{0.5}Sr_{0.5}FeO_{3-\delta}$ cathode with a nonmetal cation-doping strategy for high-performance proton-conducting solid oxide fuel cells. *SusMat* 2022, **2**: 607–616.
[55] Hu T, Xu YS, Xu K, *et al.* Visiting the roles of Sr- or Ca- doping on the oxygen reduction reaction activity and stability of a perovskite cathode for proton conducting solid oxide fuel cells. *SusMat* 2023, **3**: 91–101.
[56] Dai HL, Yin YR, Li XM, *et al.* A new Sc-doped $La_{0.5}Sr_{0.5}MnO_{3-\delta}$ cathode allows high performance for proton-conducting solid oxide fuel cells. *Sustain Mater Technol* 2022, **32**: e00409.
[57] Fabbri E, Pergolesi D, Traversa E. Materials challenges toward proton-conducting oxide fuel cells: A critical review. *Chem Soc Rev* 2010, **39**: 4355–4369.
[58] Yin YR, Xiao DD, Wu S, *et al.* A real proton-conductive, robust, and cobalt-free cathode for proton-conducting solid oxide fuel cells with exceptional performance. *SusMat* 2023, **3**: 697–708.
[59] Liu B, Li ZB, Yang XW, *et al.* Novel mixed $H^+/e^-/O^{2-}$ conducting cathode material $PrBa_{0.9}K_{0.1}Fe_{1.9}Zn_{0.1}O_{5+\delta}$ for proton-conducting solid oxide fuel cells. *J Mater Chem A* 2022, **10**: 17425–17433.
[60] Fabbri E, Pergolesi D, Licoccia S, *et al.* Does the increase in Y-dopant concentration improve the proton conductivity of $BaZr_{1-x}Y_xO_{3-\delta}$ fuel cell electrolytes. *Solid State Ionics* 2010, **181**: 1043–1051.
[61] Ren RZ, Wang ZH, Meng XG, *et al.* Tailoring the oxygen vacancy to achieve fast intrinsic proton transport in a perovskite cathode for protonic ceramic fuel cells. *ACS Appl Energy Mater* 2020, **3**: 4914–4922.
[62] Xi XA, Liu JW, Luo WZ, *et al.* Unraveling the enhanced kinetics of $Sr_2Fe_{1+x}Mo_{1-x}O_{6-\delta}$ electrocatalysts for high-performance solid oxide cells. *Adv Energy Mater* 2021, **11**: 2102845.
[63] Ding HP, Xue XJ. A novel cobalt-free layered $GdBaFe_2O_{5+\delta}$ cathode for proton conducting solid oxide fuel cells. *J Power Sources* 2010, **195**: 4139–4142.
[64] Zhao L, He BB, Nian Q, *et al. In situ* drop-coated $BaZr_{0.1}Ce_{0.7}Y_{0.2}O_{3-\delta}$ electrolyte-based proton-conductor solid oxide fuel cells with a novel layered $PrBaCuFeO_{5+\delta}$ cathode. *J Power Sources* 2009, **194**: 291–294.
[65] Mao XB, Yu T, Ma GL. Performance of cobalt-free double-perovskite $NdBaFe_{2-x}Mn_xO_{5+\delta}$ cathode materials for proton-conducting IT-SOFC. *J Alloys Compd* 2015, **637**: 286–290.
[66] Cai B, Song TF, Su JR, *et al.* Comparison of (Pr,Ba,Sr)$FeO_{3-\delta}$–SDC composite cathodes in proton-conducting solid oxide fuel cells. *Solid State Ionics* 2020, **353**: 115379.
[67] Huan DM, Shi N, Zhang L, *et al.* New, efficient, and reliable air electrode material for proton-conducting reversible solid oxide cells. *ACS Appl Mater Inter* 2018, **10**: 1761–1770.
[68] Zhang LL, Yin YR, Xu YS, *et al.* Tailoring $Sr_2Fe_{1.5}Mo_{0.5}O_{6-\delta}$ with Sc as a new single-phase cathode for proton-conducting solid oxide fuel cells. *Sci China Mater* 2022, **65**: 1485–1494.
[69] Yin YR, Wang YF, Yang N, *et al.* Unveiling the importance of the interface in nanocomposite cathodes for proton-conducting solid oxide fuel cells. *Exploration* 2024, **4**: 20230082.
[70] Bian WJ, Wu W, Wang BM, *et al.* Revitalizing interface in protonic ceramic cells by acid etch. *Nature* 2022, **604**: 479–485.
[71] Li XY, Chen ZM, Yang Y, *et al.* Highly stable and efficient Pt single-atom catalyst for reversible proton-conducting solid oxide cells. *Appl Catal B Environ* 2022, **316**: 121627.
[72] Chen C, Wang ZF, Miao XY, *et al.* Cycling performance and interface stability research of tubular protonic reversible solid oxide cells with air electrodes by different manufacturing processes. *Electrochem Commun* 2023, **151**: 107507.